ISPRS Annals of the Photogrammetry, Remote Sensing and Spatial Information Sciences, Volume X-3/W1-2022
14th GeoInformation for Disaster Management (Gi4DM 2022), 1–4 November 2022, Beijing, China

A SLAM Method for Handheld Hemispherical View Laser Scanning System

Xuzhe Duan[1], Honggang Yang[2], Qingwu Hu[1]*, Xuan Wu[2], Pengcheng Zhao[1]

[1] School of Remote Sensing and Information Engineering, Wuhan University, Wuhan, China
duanxz@whu.edu.cn, huqw@whu.edu.cn, pengcheng.zhao@whu.edu.cn
[2] China Railway Siyuan Survey and Design Group Co., LTD., Wuhan, China
003384@crfsdi.com, 327094684@qq.com

Commission III and IV

KEY WORDS: SLAM; 3D point cloud; iEKF; factor graph optimization; laser scanning system.

ABSTRACT:

In view of the problem that some multi-line light detection and ranging (LiDAR) scans a small field of view in the vertical direction, a framework that uses an integrated handheld hemispherical view LiDAR and inertial measurement unit (IMU) scanning system for simultaneous localization and mapping (SLAM) is proposed. For the structural characteristics of the hemispherical view LiDAR scan lines, a ground segmentation pre-processing module based on seed points is designed. The segmented ground points are downsampled to eliminate redundant vertical constraints. The IMU data and the pre-processed point cloud are performed state estimation via a tightly coupled iterative Extended Kalman Filter (iEKF) to obtain the real-time poses. The detected loop closures provide global constraints for the point cloud map. The factor graph is used to process the back-end optimization incrementally to eliminate the accumulation error of the system. Data from diverse scenes are collected via a prototype system. Both qualitative and quantitative experiments are performed to prove the accuracy and performance of the framework. Experiments show that our framework outperforms the state-of-the-art SLAM methods for the hemispherical view LiDAR-IMU integrated scanning system.

1. INTRODUCTION

Light detection and ranging (LiDAR) is a technique for determining accurate distances between laser scanners and object surfaces based on the time of light propagation. Depending on whether the station is fixed, LiDAR systems can be divided into two categories including Terrestrial Laser Scanning (TLS) and Mobile Laser Scanning (MLS). Among MLS, the handheld laser scanning (HLS) system is widely used in 3D mapping (Makkonen *et al.*, 2015; Duan *et al.*, 2022), architectural modeling (Hu, Wang and Xu, 2016; Previtali, Banfi and Brumana, 2020), heritage reconstruction (Zlot *et al.*, 2014; Chan *et al.*, 2016), and other scenes. Typically, LiDARs on HLS can be classified into three categories: mechanical LiDAR, solid-state LiDAR, and mixed solid-state LiDAR (Chen and Shi, 2019). Among them, the mixed solid-state LiDAR utilizes Micro Electromechanical Systems (MEMS) mirrors to reflect lasers at different angles while keeping the laser transmitter stationary. This type of LiDAR is widely integrated into autonomous vehicles profiting from its balance between cost and accuracy.

A stable and robust Simultaneous Localization and Mapping (SLAM) algorithm plays a fundamental role in estimating the six degrees of freedom (DOF) ego-motion of HLS in GNSS-denied environment. Over the past few years, LiDAR Odometry and Mapping (LOAM) (Zhang and Singh, 2014) has been considered the most classical 3D laser SLAM method. It extracts edge and surface features from scan lines based on the local smoothness. The ego-motion is then estimated by jointly optimizing point-to-edge and point-to-surface metrics using the Levenberg-Marquardt method. Thereafter, LeGO-LOAM (Shan and Englot, 2018), a variant of the LOAM method, was proposed. In LeGO-LOAM, a ground point extraction method, an image-based point cloud segmentation method, and a loop closure module are applied to improve the accuracy of LOAM. The authors of LeGO-LOAM further fused LOAM with IMU pre-integration and factor graph, and proposed LIO-SAM (Shan *et al.*, 2020) which is a tightly coupled LiDAR-inertial odometry method. Literature (Ye, Chen and Liu, 2019) proposed a LiDAR-IMU tightly coupled LIOM by replacing the image process in vision with feature extraction in LOAM, drawing on the idea of joint state estimation of vision and inertial observations in (Qin, Li and Shen, 2018). Literature (Xu and Zhang, 2021) adopted an iterated extended Kalman filter to mitigate linearization errors and presented a new formula to compute the Kalman gain to lower the computation load. Their team has also subsequently proposed an improved FAST-LIO (Xu *et al.*, 2022). This method achieves superior performance by maintaining a map with an *ikd-Tree* structure, which enables incremental updates and dynamic re-balancing.

The typical design schemes for HLS systems include (1) mounting a multi-line 360° LiDAR horizontally, as shown in Figure 1(a), and (2) mounting a LiDAR with a small field of view facing forward, as shown in Figure 1(b). Both scanning systems and their corresponding SLAM algorithms ignore the importance of acquiring sufficient scan points in the vertical direction.

(a) (b)

Figure 1. Two Classic handheld laser scanning system design solutions (Shan *et al.*, 2020)

To address this problem, this paper proposes a SLAM method for hemispherical view LiDAR scanning to achieve a larger field of view by expanding the vertical view via a 180° hemispherical view LiDAR. The SLAM method is designed according to the scan line structure characteristics of the hemispherical view LiDAR to achieve lightweight and portable handheld 3D mapping.

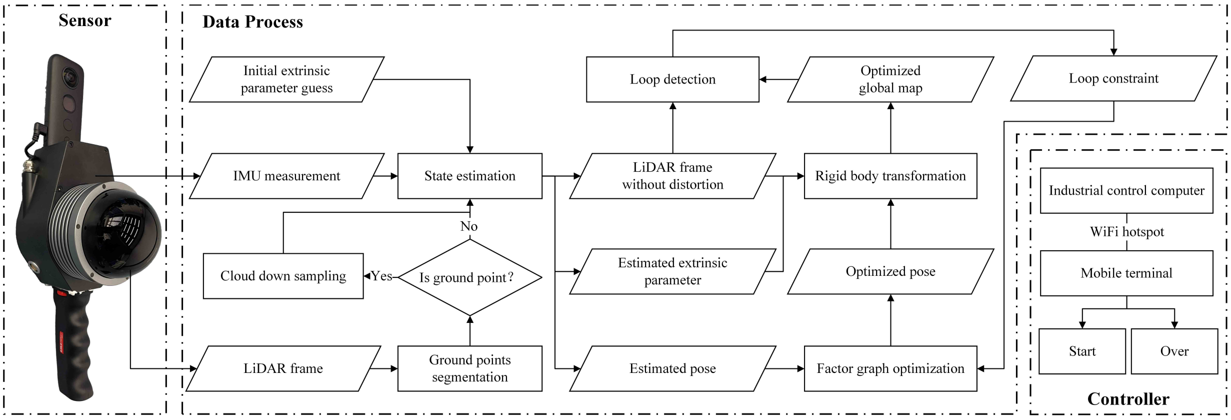

Figure 2. Workflow chart of the handheld hemispherical view laser scanning system SLAM method.

2. METHODOLOGY

We build a workable handheld hemispherical view laser scanning system prototype, as shown in Figure 2. The point cloud acquired by the hemispherical view LiDAR is first pre-processed for ground points down sampling and subsequently combined with the IMU measurement for the state estimation. The LiDAR frame without distortion, the extrinsic parameters, and the system's six DOF poses can be estimated consequently. The detected closed-loops will be added to the factor graph optimization module to construct a globally consistent 3D point cloud map.

2.1 System Overview

The handheld hemispherical view laser scanning system integrates a nine-axis IMU (Owllmo IMU3910), a hemispherical view LiDAR (RoboSense RS-Bpearl), a synchronization control board, an industrial control computer, and a power module, as shown in Figure 3.

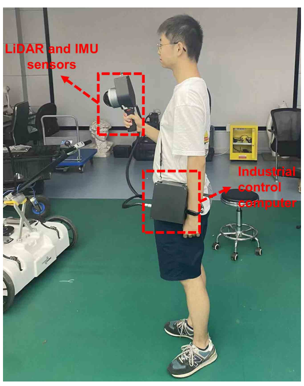

Figure 3. Handheld hemispherical view laser scanning system prototype.

The Owllmo IMU3910 consists of a gyroscope, an accelerometer, a magnetometer, and other proprioceptive sensors. The gyroscope can maintain a bias instability of 2.5×10^{-5} rad/s and a random walk of 1.2×10^{-3} rad/s, and the accelerometer can maintain a bias instability of 1.0×10^{-4} m/s^2 and a random walk of 1.3×10^{-2} m/s^2 at a maximum operating frequency of 500 Hz. The RoboSense RS-Bpearl is a LiDAR with a 360° × 90° super wide field of view (FOV). In its body coordinate system, the LiDAR can scan 360° with a maximum resolution of 0.2° in the horizontal direction and 90° with a resolution of 2.81° in the vertical direction. The distinctive hemispherical shape results in its 32 scan lines distributed in concentric circles. The LiDAR can scan up to a 100m range at an optional 10Hz or 20Hz frame rate. Mounted directly in front of the handheld system, it can effectively provide maximum data capture of the user-facing scenes. The IMU and the hemispherical view LiDAR are fixed under strict industry standards. The data acquisition terminal is connected to a portable industrial control computer with an Intel Core i7-8565U central processing unit (CPU) which strongly supports the SLAM algorithm. The system is powered by a DJI TB48S intelligent battery which has such a long life that can be used in large-scale scenes.

2.2 Ground Segmentation

Extracting feature points in the original scanned point cloud is a popular solution to reduce computational effort (Zhang and Singh, 2014; Lin and Zhang, 2020). The number and quality of feature points will directly affect the accuracy of SLAM. In most scenes, the single-frame point cloud scanned by hemispherical view LiDAR has a relatively large proportion of points falling on the ground. Figure 4 shows the distribution characteristics in a typical scene. Once the feature extraction is performed without classification, the non-ground feature points will be further reduced. In this paper, we segment out the ground points and downsample them to ensure a more uniform distribution of the single-frame scanned point cloud in space.

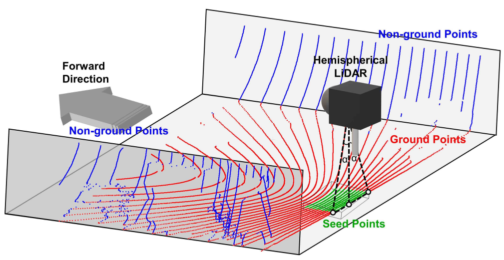

Figure 4. Ground segmentation for a forward-mounted hemispherical view LiDAR.

We suppose that the scan points in the area directly under the handheld system will fall on the planar ground. The ground seed points are selected according to the following principles: In the forward direction of the LiDAR, the outermost M scan lines are selected as the candidate scan lines; On the candidate scan lines, the points with an included angular of less than α from the direction under the handheld system are selected as the seed points (green points in Figure 4). The principal component analysis (PCA) method is utilized to extract planar parameters from the seed points (Li, Li and Hanebeck, 2021). The eigenvalue decomposition is performed on the covariance matrix of the seed points as

$$\boldsymbol{\Sigma}^s \boldsymbol{V}=\boldsymbol{V}\boldsymbol{\Lambda} \tag{1}$$

where $\boldsymbol{\Sigma}^s$ is the covariance matrix, $\boldsymbol{V}=[\boldsymbol{V_1}, \boldsymbol{V_2}, \boldsymbol{V_3}]$ is the matrix composed of eigenvectors, and $\boldsymbol{\Lambda}$ is the diagonal matrix with eigenvalues in descending order (i.e., $\lambda_1 \geq \lambda_2 \geq \lambda_3$). If λ_2 is significantly larger than λ_3 (i.e., $\lambda_3/\lambda_2 < 0.3$), the seed points are confirmed to form a plane whose normal vector is the feature direction $\boldsymbol{V_n}=\boldsymbol{V_3}$. Let the centroid of the seed points be $\boldsymbol{\mu^s}$, the distance from a point $\boldsymbol{p}$ to the seed plane can be calculated as

$$dis = (\boldsymbol{\mu^s} - \boldsymbol{p}) \cdot \boldsymbol{V_n}/|\boldsymbol{V_n}| \tag{2}$$

This distance metric is calculated for each point in a scan. The points with a distance less than the threshold dis_{τ_i} are classified as ground points. Considering the beam-directing noise of LiDARs, dis_{τ_i} is defined as a threshold that increases linearly with the detection range.

$$dis_{\tau_i} = \sigma \times |\boldsymbol{p_i}| \tag{3}$$

The number of candidate scan lines M, the seed point angle threshold α, and the distance factor σ are the parameters of the ground point segmentation algorithm, which can be adjusted according to the actual scanning scene. The point cloud is downsampled using the voxel grid method. The centroid of all points in the voxel is used to approximate the other points, which reduces the redundant ground points and improves the operation efficiency of the algorithm while ensuring the number of non-ground points remains unchanged.

2.3 State Estimation

The state estimation module is a tightly coupled iterative extended Kalman filter. Taking the first IMU frame (denoted as I) as the global frame (denoted as G), we denote the state of the handheld system as

$$\boldsymbol{x}=[\ {}^G\boldsymbol{T}_I^{\mathrm{T}} \quad {}^G\boldsymbol{v}_I^{\mathrm{T}} \quad \boldsymbol{b}_\omega^{\mathrm{T}} \quad \boldsymbol{b}_{\mathrm{a}}^{\mathrm{T}} \quad {}^G\boldsymbol{g}^{\mathrm{T}} \quad {}^I\boldsymbol{T}_L^{T}] \tag{4}$$

where ${}^G\boldsymbol{T}_I = [\ {}^G\boldsymbol{R}_I \ \ {}^G\boldsymbol{p}_I]$ is the global orientation and position of the IMU, ${}^G\boldsymbol{v}_I$ is the global velocity of the IMU, $\boldsymbol{b}_\omega$ and $\boldsymbol{b}_{\mathrm{a}}$ are IMU biases, ${}^G\boldsymbol{g}$ is the global gravity, and ${}^I\boldsymbol{T}_L = [\ {}^I\boldsymbol{R}_L \ \ {}^I\boldsymbol{p}_L]$ is the extrinsic parameters between LiDAR and IMU.

First, the prior state $\widehat{\boldsymbol{x}}_k$ and the covariance $\widehat{\boldsymbol{P}}_k$ corresponding to the kth laser scan frame are calculated according to the kinematic equations and the error propagation law. Then, the five points nearest to the prior position of the current scan point are searched in the history scan frames to form a local plane patch, and the point-to-plane distance is calculated as

$$d_j = \ {}^G\boldsymbol{u}_j^{\mathrm{T}}(\ {}^G\widehat{\boldsymbol{p}}_j - \ {}^G\boldsymbol{q}_j) \tag{5}$$

where ${}^G\boldsymbol{u}_j$ is the normal vector of the corresponding plane, ${}^G\boldsymbol{q}_j$ is the centroid of the corresponding plane, and ${}^G\widehat{\boldsymbol{p}}_j = {}^G\widehat{\boldsymbol{T}}_{I_k}\ {}^I\widehat{\boldsymbol{T}}_{L_k}\ {}^L\boldsymbol{p}_j$ is the prior position of the current scanning point in the global coordinate system. The residual calculation model shown in (6) is constructed by fusing the prior state with the point-to-plane distance and linearizing at the currently updated state $\overline{\boldsymbol{x}}_k$.

$$\begin{aligned} 0 &= \mathrm{h}_j(\boldsymbol{x}_k,\ {}^L\boldsymbol{n}_j) \\ &\approx \mathrm{h}_j(\widehat{\boldsymbol{x}}_k, 0) + \boldsymbol{H}_j(\boldsymbol{x}_k \boxminus \overline{\boldsymbol{x}}_k) + \boldsymbol{w}_j \\ &= {}^G\boldsymbol{u}_j^{\mathrm{T}}(\ {}^G\widehat{\boldsymbol{p}}_j - \ {}^G\boldsymbol{q}_j) + \boldsymbol{H}_j(\boldsymbol{x}_k \boxminus \overline{\boldsymbol{x}}_k) + \boldsymbol{w}_j \\ &= \boldsymbol{z}_j + \boldsymbol{H}_j(\boldsymbol{x}_k \boxminus \overline{\boldsymbol{x}}_k) + \boldsymbol{w}_j \end{aligned} \tag{6}$$

where $\boxminus$ is the encapsulation operation that act on manifolds, $\boldsymbol{H}_j$ is the Jacobian matrix of $\mathrm{h}_j(\boldsymbol{x}_k,\ {}^L\boldsymbol{n}_j)$ with respect to $\widehat{\boldsymbol{x}}_k$, and $\boldsymbol{w}_j \in \mathcal{N}(0, \boldsymbol{R}_j)$ is the raw observation noise (Xu *et al.*, 2022). Finally, combining the prior and observation yields the maximum a posterior (MAP) estimation problem as

$$\min_{\boldsymbol{x}_k \boxminus \overline{\boldsymbol{x}}_k} \left(\|\boldsymbol{x}_k \boxminus \widehat{\boldsymbol{x}}_k\|^2_{\widehat{\boldsymbol{P}}_k} + \textstyle\sum_{j=1}^{m} \|\boldsymbol{z}_j + \boldsymbol{H}_j(\boldsymbol{x}_k \boxminus \overline{\boldsymbol{x}}_k)\|^2_{\boldsymbol{R}_j} \right) \tag{7}$$

The first half represents the prior of the state and the second half represents the observation residual. This MAP problem is solved by iterated Kalman filter on manifolds. The converged state estimate $\overline{\boldsymbol{x}}_k$ and the Hessian matrix $\overline{\boldsymbol{P}}_k$ yield the pose output and continue to propagate the incoming IMU measurements.

2.4 Factor Graph Optimization and Mapping

To eliminate the drift caused by long-time error accumulation, this paper uses the factor graph to conduct back-end optimization. The Scan Context method is used for loop-closure detection (Kim and Kim, 2018). As shown in Figure 5, the state of the system is considered to be optimized and is incrementally inserted into the factor graph in the form of variable nodes. The pose information estimated in the previous step provides inter-frame constraints, and the loop-closure frames are matched with the historical local submap to provide loop constraints. The constraints are inserted between the variable nodes in the form of factor nodes.

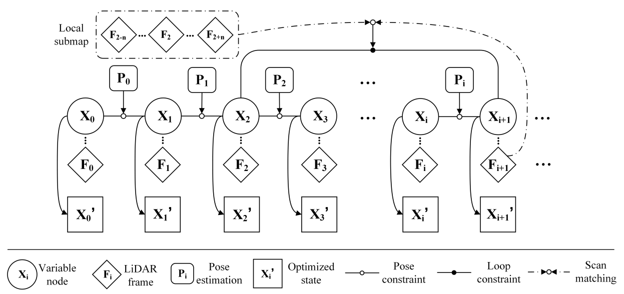

Figure 5. Schematic diagram of factor graph optimization

The factor graph is optimized via the incremental smoothing and mapping method. Each time a new LiDAR observation is received triggers the optimization computation, the window keeps sliding forward and the factor graph maintains a fixed number of nodes, thus ensuring the efficiency of the optimization computation (Kaess *et al.*, 2012). The factor graph is transformed into the nonlinear function

$$\min_{x_i} \left(\textstyle\sum \widehat{\boldsymbol{C}}^p_{i-1,i} + \sum \widehat{\boldsymbol{C}}^l_{k,i} \right) \tag{8}$$

where $\widehat{\mathcal{C}}^p$ and $\widehat{\mathcal{C}}^l$ are the nodes corresponding to the inter-frame constraints and the loop constraints, respectively. The optimal estimate of each variable node is solved using the Levenberg-Marquardt method to obtain globally consistent poses. Using the LiDAR-IMU extrinsic parameters and the system poses optimized by the factor map, the real poses of the scanned points can be restored by rigid body transformation of the point cloud frame without distortion. Finally, the point cloud is accumulated frame by frame in the global coordinate system to obtain the 3D point cloud map of the whole scene.

3. EXPERIMENTS

A series of datasets in indoor and outdoor scenes are logged to evaluate our proposed framework qualitatively and quantitatively. Some of the experimental data are collected in GNSS-denied environments by a user holding the handheld LiDAR system with hand, while other data are collected in open-air environments by fixing the system on a mobile platform equipped with a GNSS + Inertial Navigation System (INS) system, as shown in Figure 6.

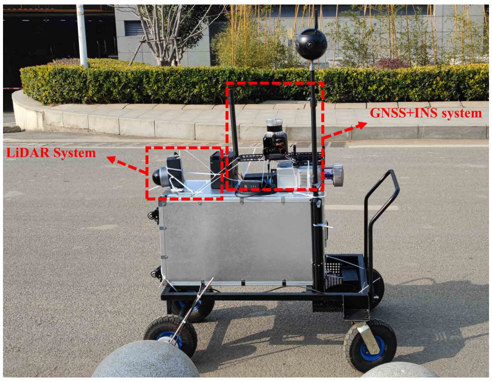

Figure 6. The equipment for outdoor data collection

In the qualitative experiments, we verify the fineness of point cloud objects and the compatibility of point cloud maps with Google Earth images. In the quantitative experiments, we evaluate the accuracy of the trajectory with the good quality GNSS ground truth and conduct a runtime analysis of the framework. See Table I for details of the datasets. Note that all experiments are executed on the industrial control computer equipped with an Intel i7-8565U using the robot operating system (ROS) (Quigley *et al.*, 2009) in Ubuntu Linux.

Dataset	Frames	Duration (*s*)	Length (*m*)	GNSS
Indoor 1	2266	226.63	218.39	unavailable
Indoor 2	1252	125.29	54.63	unavailable
Outdoor 1	3306	330.72	335.59	unavailable
Outdoor 2	3414	341.45	422.25	unavailable
Outdoor 3	9530	953.00	869.16	available
Outdoor 4	5667	566.75	573.64	available

Table 1. Dataset details.

3.1 Point Cloud Details

We evaluate the fineness of the indoor point clouds by comparing the detail of the point cloud objects generated by LOAM (Zhang and Singh, 2014), LIOM (Ye, Chen and Liu, 2019), and Ours, as shown in Figure 7. These point clouds are rendered by the intensity values.

In the *Indoor 1* dataset, we select a car that is scanned over a large area as the study object. Compared to our algorithm (Figure 7(c)), the point clouds of the car generated by the LOAM (Figure 7(a)) and LIOM (Figure 7(b)) have significant discrete noise (especially around the rear of the car). The details such as the license plate and the car lights distinguished based on the intensity information are more markable in our algorithm. In the *Indoor 2* dataset, a chair scanned at several angles is selected as the observation object. The chair generated by LOAM (Figure 7(d)) is blurred and has obvious distortion at the backrest; the chair generated by LIOM (Figure 7(e)) produces misalignment in the vertical direction, and the ground is misclassified into two planes; the chair generated by our algorithm (Figure 7(f)) ensures both consistency in the whole and uniformity and delicacy in the details and the intensity information can be used to distinguish the chair armrests and backrests. The above comparison shows that the algorithm of this paper performs better in the fineness and uniformity of the point cloud.

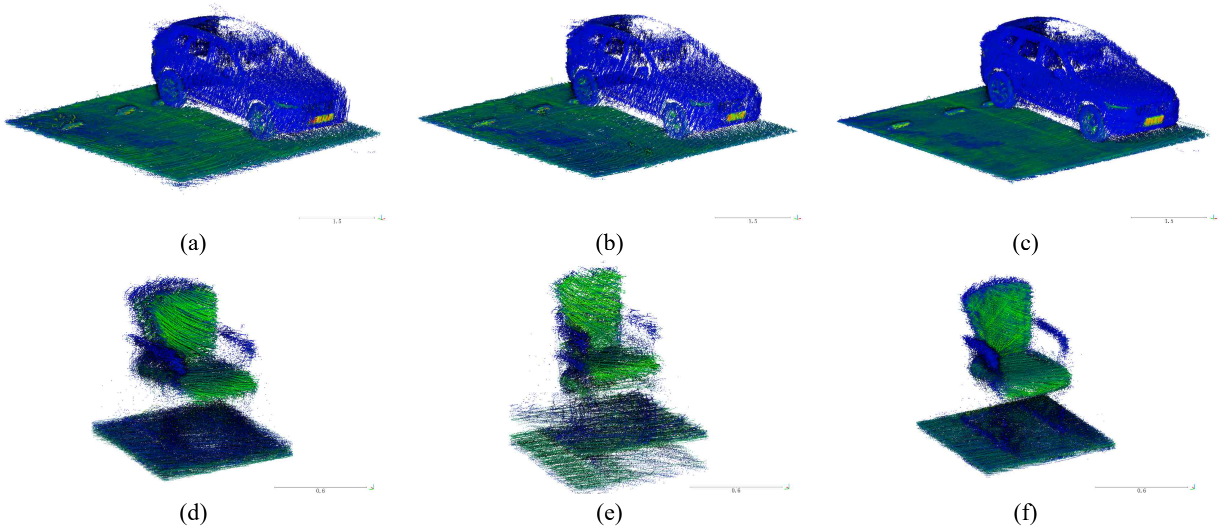

Figure 7. The comparison of point cloud details. (a) the car generated by LOAM; (b) the car generated by LIOM; (c) the car generated by Ours; (d) the chair generated by LOAM; (e) the chair generated by LIOM; (f) the chair generated by Ours.

3.2 Point Clouds Aligned with Google Earth Images

Figure 8 shows the point cloud maps aligned with Google Earth images via our algorithm. The bird's eye view point cloud map and the 3D point cloud details are rendered according to the height values and the intensity values, respectively. In the *Outdoor 1* dataset and *Outdoor 2* dataset, the instability of handheld does not cause the point cloud maps to drift significantly. Landmarks such as bushes, corridors, and buildings can be well aligned with real scenes. Our algorithm also conquers the challenges posed by the open environment of the *Outdoor 3* dataset and *Outdoor 4* dataset and still shows excellent performance in long-distance scenes.

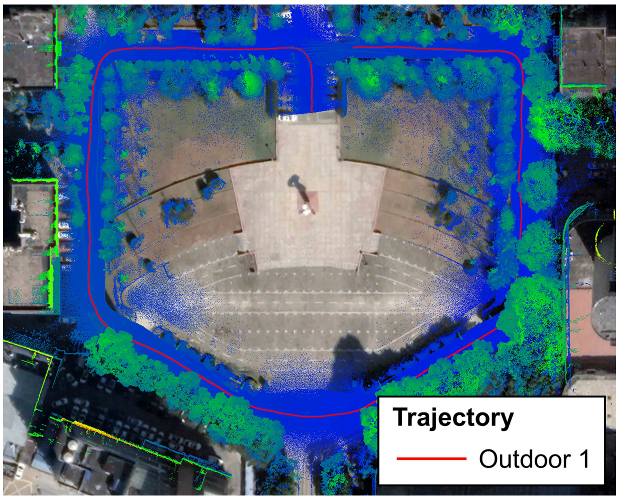

(a) *Outdoor 1* dataset

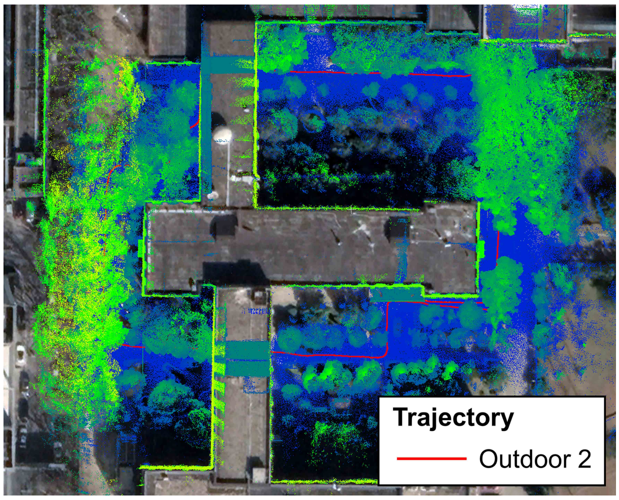

(b) *Outdoor 2* dataset

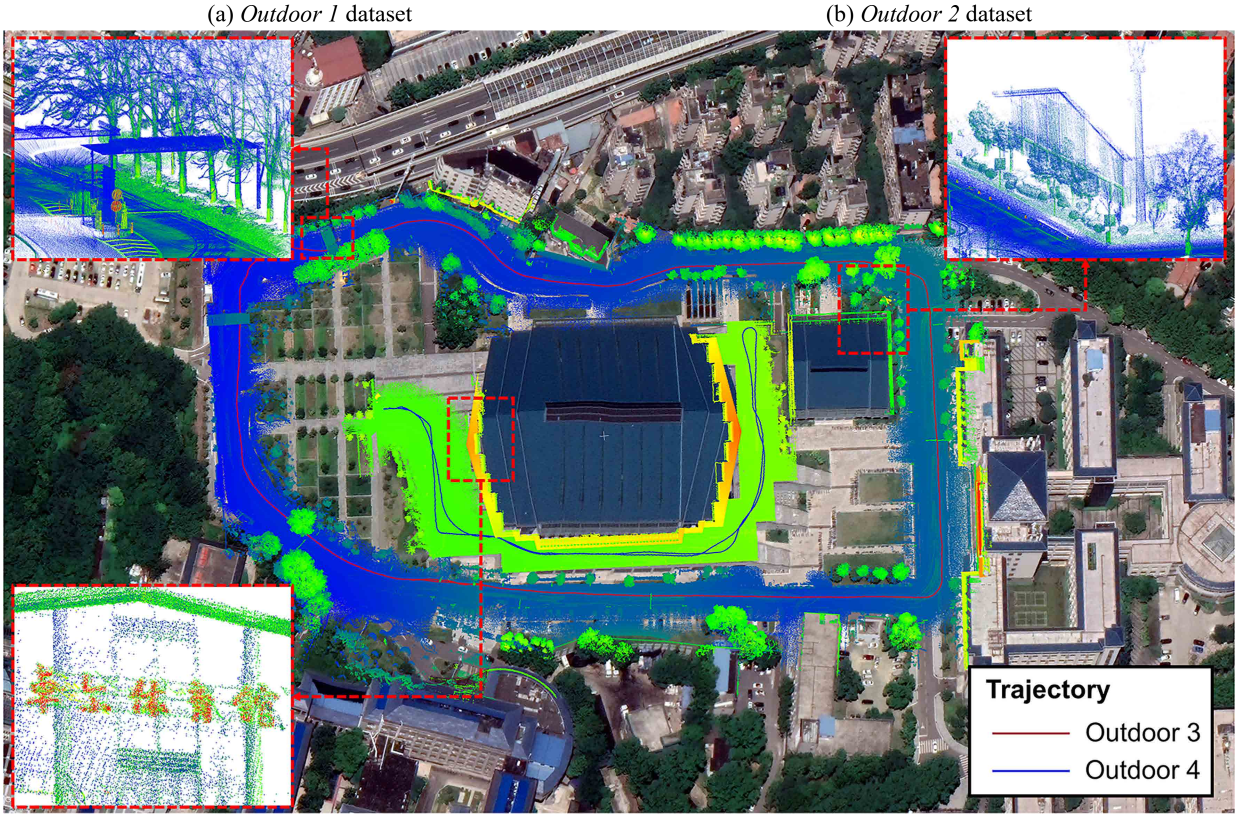

(c) *Outdoor 3* dataset and *Outdoor 4* dataset

Figure 8. Point clouds aligned with Google Earth images.

3.3 Trajectory Accuracy Evaluation

Outdoor datasets with high-quality ground truths are applied for quantitative experiments. We test the *Outdoor* 3 dataset and the *Outdoor* 4 dataset via LOAM (Zhang and Singh, 2014), LIOM (Ye, Chen and Liu, 2019), FAST-LIO (Xu and Zhang, 2021; Xu *et al.*, 2022), and Ours, respectively. We utilize two prominent indicators including the absolute trajectory error (ATE) and the relative pose error (RPE) for accuracy analysis. The root mean square error (RMSE) of the ATE and the RPE are reported in Table 2, in which the ratio error represents the ratio of ATE or RPE to the length of the trajectory. The ablation studies are performed by separately supplementing the ground points down sampling course and the loop closure optimization course

https://doi.org/10.5194/isprs-annals-X-3-W1-2022-37-2022 | © Author(s) 2022. CC BY 4.0 License.

(denoted as FAST-LIO-GD and FAST-LIO-L, respectively) to FAST-LIO. The results show that an individual ground points down sampling course or loop closure optimization course is of value to reduce the trajectory error of FAST-LIO and that the best trajectory accuracy is achieved by combining both in our improved algorithm. In the *Outdoor 4* dataset, the trajectory error of our algorithm increases a bit compared with the FAST-LIO-GD, probably since there is no effective closed-loop during the actual data acquisition process. Nonetheless, this does not detract from the fact that the improved algorithm is better suited to our system than the original FAST-LIO.

Dataset	Indicator	LOAM	LIOM	FAST-LIO	FAST-LIO-GD	FAST-LIO-L	Ours
Outdoor 3	ATE (*m*)	35.55	32.98	5.04	4.53	3.47	**3.45**
	ATE ratio error	4.09×10^{-2}	3.79×10^{-2}	5.80×10^{-3}	5.21×10^{-3}	3.99×10^{-3}	$\mathbf{3.97\times10^{-3}}$
	RPE (*m*)	0.31	0.25	0.19	0.18	0.19	**0.18**
	RPE ratio error	3.57×10^{-4}	2.88×10^{-4}	2.19×10^{-4}	2.07×10^{-4}	2.19×10^{-4}	$\mathbf{2.07\times10^{-4}}$
Outdoor 4	ATE (*m*)	30.22	1.25	2.20	**0.85**	2.67	0.87
	ATE ratio error	5.27×10^{-2}	2.18×10^{-3}	3.84×10^{-3}	$\mathbf{1.48\times10^{-3}}$	4.65×10^{-3}	1.52×10^{-3}
	RPE (*m*)	0.24	0.32	0.16	0.03	0.09	**0.03**
	RPE ratio error	4.18×10^{-4}	5.58×10^{-4}	2.79×10^{-4}	5.23×10^{-5}	1.57×10^{-4}	$\mathbf{5.23\times10^{-5}}$

Table 2. Trajectory accuracy evaluation.

3.4 Runtime Analysis

Runtime analysis is implemented to verify the real-time performance of the system. Compared to FAST-LIO, the main runtime consumption to be counted in our SLAM method occurs in the ground segmentation module and loop closure optimization module. Note that the loop closure optimization module is computed in parallel using *OpenMP*. A detailed runtime comparison between FAST-LIO and Ours is reported in Table 3. Our approach of segmenting and then downsampling the ground points results in fewer points remaining for subsequent computations and thus not a huge increase in runtime. The effect of this operation is particularly noticeable in outdoor scenes with a large proportion of ground points. This is the reason why the runtime of our algorithm on the outdoor dataset will be much closer to or even shorter than FAST-LIO. In conclusion, our algorithm is not significantly slower than FAST-LIO and can operate faster than 20 Hz on the industrial control computer.

Dataset	FAST-LIO	Ours
Indoor 1	28.97	35.81
Indoor 2	27.33	34.11
Outdoor 1	33.93	33.46
Outdoor 2	32.89	33.88
Outdoor 3	21.47	24.36
Outdoor 4	19.24	21.17

Table 3. Run time per frame (*ms*).

4. CONCLUSION

This paper proposes a SLAM framework using a handheld hemispherical view laser scanning system. The hemispherical view LiDAR and IMU are integrated onto the prototype as well as a data processing system is developed. Taking full advantage of the scan line features of the hemispherical view LiDAR, we design a targeted ground segmentation module and a loop closure optimization module based on the factor graph optimization. Plenty of indoor and outdoor data are collected to perform both qualitative and quantitative experiments. The results show that the proposed framework can meet the low-drift performance faster than 20 Hz per frame. Future work will be devoted to enriching the types of sensors integrated into the system, such as assembling the consumer-grade panoramic camera and simultaneously collecting the laser scans and the panoramic images. Based on the reconstruction of the 3D scene, the panoramic image will be mapped to the 3D point cloud, and the coloring of the point cloud will be realized to enhance the effect of the scene.

ACKNOWLEDGEMENTS

This work is supported by the National Key R&D Program of China (No. 2021YFB2600401), the National Natural Science Foundation of China (NSFC) (No. 42101441), and the Fundamental Research Funds for the Central Universities.

REFERENCES

Chan, T. *et al.* (2016) "Survey Accuracy Analysis of a Hand-held Mobile LiDAR Device for Cultural Heritage Documentation," *Photogrammetrie - Fernerkundung - Geoinformation*, 2016, pp. 153–165. Available at: https://doi.org/10.1127/pfg/2016/0294.

Chen, J. and Shi, Y. (2019) "Research progress in solid-state LiDAR," *Guangdian Gongcheng/Opto-Electronic Engineering*. Chinese Academy of Sciences. Available at: https://doi.org/10.12086/oee.2019.190218.

Duan, X. *et al.* (2022) "A Low-Cost and Portable Indoor 3D Mapping Approach Using Biaxial Line Laser Scanners and a One-Dimension Laser Range Finder Integrated with Microelectromechanical Systems," *Photogrammetric Engineering & Remote Sensing*, 88(5), pp. 311–321. Available at: https://doi.org/10.14358/PERS.21-00037R2.

Hu, S., Wang, D. and Xu, S. (2016) "3D indoor modeling using a hand-held embedded system with multiple laser range scanners," in S. Han and J. Tan (eds) *Optical Measurement Technology and Instrumentation*. SPIE, pp. 620 – 625. Available at: https://doi.org/10.1117/12.2247006.

Kaess, M. *et al.* (2012) "iSAM2: Incremental Smoothing and Mapping Using the Bayes Tree," *International Journal of Robotic Research - IJRR*, 31, pp. 216–235. Available at: https://doi.org/10.1177/0278364911430419.

Kim, G. and Kim, A. (2018) "Scan Context: Egocentric Spatial Descriptor for Place Recognition Within 3D Point Cloud Map," in *2018 IEEE/RSJ International Conference on Intelligent Robots and Systems (IROS)*, pp. 4802–4809. Available at: https://doi.org/10.1109/IROS.2018.8593953.

Li, K., Li, M. and Hanebeck, U.D. (2021) "Towards High-Performance Solid-State-LiDAR-Inertial Odometry and Mapping," *IEEE Robotics and Automation Letters*, 6(3), pp. 5167–5174. Available at: https://doi.org/10.1109/LRA.2021.3070251.

Lin, J. and Zhang, F. (2020) "Loam livox: A fast, robust, high-precision LiDAR odometry and mapping package for LiDARs of small FoV," in *2020 IEEE International Conference on Robotics and Automation (ICRA)*, pp. 3126–3131. Available at: https://doi.org/10.1109/ICRA40945.2020.9197440.

Makkonen, T. *et al.* (2015) "The Applicability of the Rapid Handheld Laser Scanner to Underground Tunnel Suveying," in M. Malaska and R. Heikkilä (eds) *Proceedings of the 32nd International Symposium on Automation and Robotics in Construction and Mining (ISARC 2015)*. Oulu, Finland: International Association for Automation and Robotics in Construction (IAARC), pp. 1–7. Available at: https://doi.org/10.22260/ISARC2015/0107.

Previtali, M., Banfi, F. and Brumana, R. (2020) "Handheld 3D Mobile Scanner (SLAM): Data Simulation and Acquisition for BIM Modelling," in, pp. 256–266. Available at: https://doi.org/10.1007/978-3-030-62800-0_20.

Qin, T., Li, P. and Shen, S. (2018) "VINS-Mono: A Robust and Versatile Monocular Visual-Inertial State Estimator," *IEEE Transactions on Robotics*, 34(4), pp. 1004–1020. Available at: https://doi.org/10.1109/TRO.2018.2853729.

Quigley, M. *et al.* (2009) "ROS: an open-source Robot Operating System," in *ICRA Workshop on Open Source Software*.

Shan, T. *et al.* (2020) "LIO-SAM: Tightly-coupled Lidar Inertial Odometry via Smoothing and Mapping," in *2020 IEEE/RSJ International Conference on Intelligent Robots and Systems (IROS)*, pp. 5135–5142. Available at: https://doi.org/10.1109/IROS45743.2020.9341176.

Shan, T. and Englot, B. (2018) "LeGO-LOAM: Lightweight and Ground-Optimized Lidar Odometry and Mapping on Variable Terrain," in *2018 IEEE/RSJ International Conference on Intelligent Robots and Systems (IROS)*, pp. 4758–4765. Available at: https://doi.org/10.1109/IROS.2018.8594299.

Xu, W. *et al.* (2022) "FAST-LIO2: Fast Direct LiDAR-Inertial Odometry," *IEEE Transactions on Robotics*, pp. 1–21. Available at: https://doi.org/10.1109/TRO.2022.3141876.

Xu, W. and Zhang, F. (2021) "FAST-LIO: A Fast, Robust LiDAR-Inertial Odometry Package by Tightly-Coupled Iterated Kalman Filter," *IEEE Robotics and Automation Letters*, 6(2), pp. 3317–3324. Available at: https://doi.org/10.1109/LRA.2021.3064227.

Ye, H., Chen, Y. and Liu, M. (2019) "Tightly Coupled 3D Lidar Inertial Odometry and Mapping," in *2019 International Conference on Robotics and Automation (ICRA)*, pp. 3144–3150. Available at: https://doi.org/10.1109/ICRA.2019.8793511.

Zhang, J. and Singh, S. (2014) "LOAM: Lidar Odometry and Mapping in Real-time," in *Proceedings of Robotics: Science and Systems (RSS '14)*.

Zlot, R. *et al.* (2014) "Efficiently capturing large, complex cultural heritage sites with a handheld mobile 3D laser mapping system," *Journal of Cultural Heritage*, 15(6), pp. 670–678. Available at: https://doi.org/https://doi.org/10.1016/j.culher.2013.11.009.